HHS Public Access

Author manuscript

Science. Author manuscript; available in PMC 2024 December 02.

Published in final edited form as:

Science. 2024 August 30; 385(6712): eadj8691. doi:10.1126/science.adj8691.

Micronuclear collapse from oxidative damage

Melody Di Bona[1,2], **Yanyang Chen**[3,†], **Albert S. Agustinus**[1,2,4,†], **Alice Mazzagatti**[5], **Mercedes A. Duran**[1,2], **Matthew Deyell**[6], **Daniel Bronder**[1,2], **James Hickling**[3], **Christy Hong**[1,2], **Lorenzo Scipioni**[7,8], **Giulia Tedeschi**[7,8], **Sara Martin**[9,§], **Jun Li**[1,2], **Aušrinė Ruzgaitė**[1,2], **Nadeem Riaz**[1], **Parin Shah**[10], **Edridge K. D'Souza**[10], **D. Zack Brodtman**[10], **Simone Sidoli**[11], **Bill Diplas**[1], **Manisha Jalan**[1], **Nancy Y. Lee**[1], **Alban Ordureau**[12], **Benjamin Izar**[10], **Ashley M. Laughney**[6], **Simon Powell**[1], **Enrico Gratton**[7], **Stefano Santaguida**[9,13], **John Maciejowski**[3], **Peter Ly**[5], **Thomas M. Jeitner**[14], **Samuel F. Bakhoum**[1,2,*]

[1]Department of Radiation Oncology, Memorial Sloan Kettering Cancer Center, New York, NY 10065, USA

[2]Human Oncology and Pathogenesis Program, Memorial Sloan Kettering Cancer Center, New York, NY 10065, USA

[3]Molecular Biology Program, Memorial Sloan Kettering Cancer Center, New York, NY 10065, USA

[4]Pharmacology Graduate Program, Weill Cornell Medicine, New York, NY 10065, USA

[5]Department of Pathology, University of Texas Southwestern Medical Center, Dallas, TX 75390, USA

[6]Department of Physiology, Biophysics and Systems Biology, Weill Cornell Medicine, New York, NY 10065, USA

[7]School of Engineering, University of California, Irvine, CA 92697, USA

[8]Laboratory for Fluorescence Dynamics, University of California, Irvine, Irvine, CA 92617, USA

[*]**Corresponding author.** samuel.bakhoum@gmail.com.

[†]These authors contributed equally to this work.

[§]Present address: Axxam S.p.A., Milan, Italy.

Author contributions: Conceptualization: M.D.B. and S.F.B. Methodology: M.D.B., Y.C., A.S.A., A.M., M.A.D., M.D., C.H., D.B., L.S., G.T., S.M., A.R., N.R., N.Y.L., B.D., P.S., E.K.D., Z.B., S.Si., P.L., A.O., M.J., T.M.J., and J.L. Investigation: M.D.B., Y.C., M.D., M.A.D., A.M., G.T., D.B., C.H., J.H., A.O., B.D., and T.M.J. Visualization: M.D.B., S.F.B., and S.Sa. Funding acquisition: S.F.B. Supervision: S.F.B., A.L., E.G., J.M., S.P., T.J., B.I., and P.L. Writing – original draft: M.D.B., S.F.B., and T.M.J.

Competing interests: S.F.B. owns equity in, receives compensation from, serves as a consultant to, and serves on the scientific advisory board and board of directors of Volastra Therapeutics and serves on the scientific advisory board of Meliora Therapeutics. S.P. currently maintains a consultant relationship with Varian Medical Systems, from whom he receives compensation and cost of travel for his services. He also serves on the advisory board for Rain Therapeutics and receives compensation and cost of travel for those services as well. Lastly, he is a consortium participant with Varian Medical Systems and is compensated for the cost of travel expenses whenever applicable. A.O. has a consultant relationship with Nine Square Therapeutics, from whom he receives compensation and cost of travel for his services. J.M. has a planned patent related to aspects of targeting the cGAS-STING pathway in cancer-pertaining work conducted at MSKCC. N.Y.L. is on the advisory boards of Merck, Merck EMD, Nanobiotix, Galera, and LEO SAB; she has stock options in LEO SAB and has speaking/consulting duties for Varian Medical Systems, Yinming Consulting, and Shanghai JoAnn Medical Technology.

[9]Department of Experimental Oncology, European Institute of Oncology IRCCS, 20141 Milan, Italy

[10]Systems Biology Department, Columbia University, New York, NY 10032, USA

[11]Department of Biochemistry, Albert Einstein College of Medicine, New York, NY 10461, USA

[12]Cell Biology Program, Memorial Sloan Kettering Cancer Center, New York, NY 10065, USA

[13]Department of Oncology and Hemato-Oncology, University of Milan, 20122 Milan, Italy

[14]Department of Radiology, Weill Cornell Medicine, New York, NY 10065, USA

Abstract

Chromosome-containing micronuclei are a hallmark of aggressive cancers. Micronuclei frequently undergo irreversible collapse, exposing their enclosed chromatin to the cytosol. Micronuclear rupture catalyzes chromosomal rearrangements, epigenetic abnormalities, and inflammation, yet mechanisms safeguarding micronuclear integrity are poorly understood. In this study, we found that mitochondria-derived reactive oxygen species (ROS) disrupt micronuclei by promoting a noncanonical function of charged multivesicular body protein 7 (CHMP7), a scaffolding protein for the membrane repair complex known as endosomal sorting complex required for transport III (ESCRT-III). ROS retained CHMP7 in micronuclei while disrupting its interaction with other ESCRT-III components. ROS-induced cysteine oxidation stimulated CHMP7 oligomerization and binding to the nuclear membrane protein LEMD2, disrupting micronuclear envelopes. Furthermore, this ROS-CHMP7 pathological axis engendered chromosome shattering known to result from micronuclear rupture. It also mediated micronuclear disintegrity under hypoxic conditions, linking tumor hypoxia with downstream processes driving cancer progression.

INTRODUCTION: Chromosomal instability, a hallmark of aggressive cancers, is characterized by the presence of micronuclei, which are cytosolic rupture-prone structures that contain entire chromosomes or chromosome arms. The irreversible collapse of micronuclear envelopes is a central event in tumor progression. Micronuclear collapse exposes the encapsulated DNA to the cytosol, catalyzing chromosomal rearrangements and epigenetic alterations that drive tumor heterogeneity as well as therapy resistance. Micronuclear rupture also activates inflammatory signaling pathways that reshape the tumor immune microenvironment, promoting metastasis. Despite its importance, the underlying mechanisms of micronuclear collapse are unclear.

RATIONALE: Maintaining the integrity of the nuclear membrane is essential for cellular functions and organismal viability. It is unclear what cellular safeguards are compromised in micronuclei that lead to the breakdown of nuclear membrane integrity. We posited that inherent dissimilarities between micronuclei and primary nuclei might explain their respective differences in membrane stability. For instance, micronuclei are 5- to 20-fold smaller than the primary nucleus. Secondly, they possess abnormal nuclear envelopes, as evidenced by aberrant nuclear pore function and reduced lamin B1 levels. In addition, once ruptured, micronuclear envelopes are seldom repaired.

RESULTS: In this study, we integrated prior observations with our findings that micronuclear envelope rupture occurs because of the aberrant interaction between micronuclei and mitochondria, a process that is mediated by reactive oxygen species (ROS). Indeed, ruptured

micronuclei were more likely to be intermixed with the mitochondrial network compared with intact ones, and manipulation of ROS levels correspondingly altered the rates of micronuclear rupture. Subsequent proteomic analysis and genetic manipulations led us to the observation that ROS interfere with micronuclear integrity by disrupting the normal activity of the nuclear membrane repair complex known as the endosomal sorting complex required for transport III (ESCRT-III). Increases in ROS levels led to the micronuclear accumulation of the ESCRT-III scaffolding protein, charged multi-vesicular body protein 7 (CHMP7), promoting a noncanonical function. ROS inhibited the export of CHMP7, leading to its persistence in the micronucleus and aberrant binding to its inner nuclear membrane partner LEM domain nuclear envelope protein 2 (LEMD2). ROS-induced cysteine oxidation catalyzed CHMP7 aggregation and reduced its interaction with its canonical binding partners in the ESCRT-III complex. The binding of CHMP7 aggregates to LEMD2 promoted micronuclear membrane deformation and collapse. This effect was further exacerbated by ROS-dependent recruitment of the autophagy-related protein p62, which mediated the degradation of canonical ESCRT-III members, limiting any chances of subsequent membrane repair. Lastly, we found that this mechanism is relevant to human tumors. Elevated levels of ROS and aberrant CHMP7 function led to complex chromosomal rearrangements, or chromothripsis, known to arise from micronuclear rupture. Furthermore, ROS generated under hypoxia induced micronuclear rupture in a CHMP7-dependent manner. In line with these findings, we observed a significant increase in micronuclear rupture along with CHMP7 accumulation in hypoxic regions of human head and neck cancer as well as in ovarian tumors.

CONCLUSION: Our results have uncovered a pathological interaction between micronuclei and mitochondria that underlies micronuclear rupture. By implicating ROS as regulators of micronuclear integrity, this work provides a mechanistic link between ROS-inducing conditions (such as free-radical generation and hypoxia) and downstream processes known to arise from the presence of micronuclei, including chromosomal rearrangements, epigenetic dysregulation, and tumor-promoting inflammation. ■

Mechanisms of micronuclear rupture.

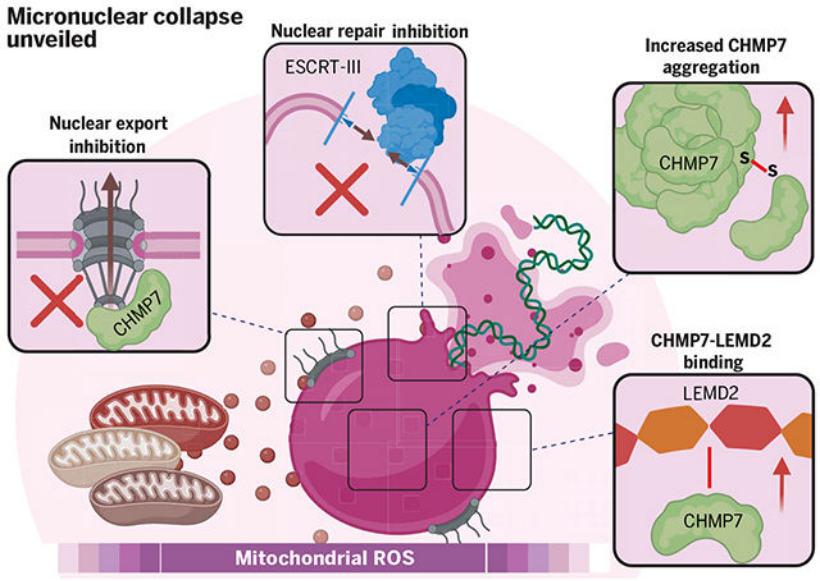

The proximity of mitochondria to micronuclei drives micronuclear membrane rupture through mitochondria-derived reactive oxygen species (ROS). ROS inhibit micronuclear export, leading to the excessive accumulation of CHMP7, a scaffolding protein associated with the nuclear membrane repair complex ESCRT-III. ROS-dependent cysteine oxidation promotes CHMP7 self-aggregation and its aberrant binding to the membrane protein LEMD2, causing micronuclear collapse. [Figure created with BioRender.com]

Mammalian cells have evolved robust mechanisms to safeguard the integrity of the nuclear envelope (1–4). Yet multiple physiological and pathological processes lead to nuclear envelope rupture, necessitating rapid repair. The endosomal sorting complex required for transport III (ESCRT-III) complex is a key player in mediating nuclear envelope repair, and it assembles through binding to LEM domain nuclear envelope protein 2 (LEMD2) and charged multivesicular body protein 7 (CHMP7) scaffolds at the nuclear membrane rupture sites (5, 6). Although membrane repair of the primary nucleus has been studied extensively, less is known about the mechanisms that regulate the integrity of chromosome-containing micronuclei. Micronuclei are a hallmark of cancer cells with chromosomal instability (CIN) (7), a feature that is associated with poor prognosis, therapeutic resistance, and distant metastasis (8–12).

Micronuclei result from mitotic errors during chromosome segregation (13, 14), and they are characterized by an aberrant nuclear envelope with reduced lamin B content (15). Unlike the primary nucleus, micronuclear envelope rupture is typically irreversible, thus exposing the enclosed chromatin to the cytoplasm (16). Micronuclear rupture has been shown to catalyze complex genomic rearrangements such as chromothripsis (17) and long-lasting epigenetic abnormalities (18, 19) that facilitate tumor evolution. In addition, ruptured micronuclei are a major source of cytosolic double-stranded DNA, which activates the cyclic GMP-AMP synthase and stimulator of interferon genes (cGAS-STING) innate immune pathway. Under normal circumstances, cGAS-STING activation mediates proinflammatory signaling that can exert antitumor activity; however, chronic activation of this pathway in chromosomally unstable tumor cells has also been shown to engender tumor-promoting inflammation, leading to metastatic progression. The irreversible nature of micronuclear collapse invokes inherent defects in membrane integrity and repair mechanisms in micronuclei that are distinct from primary nuclei (16). Recent studies have identified invasion of the endoplasmic reticulum membrane into micronuclear membranes, defective nuclear pore complex formation, and weakened micronuclear lamina as features that distinguish micronuclei from primary nuclei (15, 16, 20). Yet, the precise mechanisms underlying micronuclear rupture and deficiency at repair remain poorly understood (12, 15, 16, 21–23).

Mitochondria-derived ROS promoted micronuclear collapse

Working in HeLa cells, we observed a significant spatial overlap between micronuclei and the mitochondria (Fig. 1, A and B, and fig. S1). In addition, micronuclei that made extensive and prolonged contact with the mitochondrial network were more likely to rupture compared with those further away (Fig. 1, A to E, and fig. S1). An unbiased proteomic analysis

of primary nuclei and micronuclei revealed enrichment of mitochondria-related proteins in micronuclei (Fig. 1F and table S1). We hypothesized that proximity to mitochondria exposes micronuclei to reactive oxygen species (ROS), impacting micronuclear envelope integrity. Electron leakage from complexes I and III of the electron transport chain (ETC) constitutes the major source of mitochondria-derived ROS (24, 25). To test the involvement of ROS in rupture, we assessed the integrity of micronuclei in a panel of seven cell lines (table S2) after the addition of hydrogen peroxide (H_2O_2) or treatment with oligomycin or VLX600, known disruptors of the mitochondrial ETC (26, 27). Micronuclear integrity was assessed using multiple orthogonal approaches. The presence of lamin B1, lamin A (20), acetylated histone H3 at lysine 9 (H3K9Ac), or red fluorescent protein (RFP) fused to a nuclear localization sequence (NLS) denoted intact micronuclei. Conversely, their absence, or the presence of cGAS (28), which is rapidly recruited after loss of micronuclear membrane integrity, indicated ruptured micronuclei (Fig. 1G; fig. S2, A to S; and fig. S3, A and B). ROS levels for each of the treatment conditions were measured in cell lysates with a luminescence-based assay (fig. S3C). Induction of ROS by direct addition of H_2O_2 or disruption of the mitochondrial ETC led to a significant increase in the proportion of ruptured micronuclei with limited or no effect on the total number of micronuclei (Fig. 1, H to K, and fig. S3, D to G). Conversely, treatment of thyroid-immortalized NTHY Ori 3.1 (NTHY), osteosarcoma (U2OS), or cervical carcinoma (HeLa) cells with the cellular ROS-scavenger *N*-acetyl cysteine (NAC) (29, 30), the mitochondrial ROS-scavenger MitoQuinone (MitoQ) (31), or catalase (32) uniformly reduced the incidence of micronuclear rupture (Fig. 1, L to N, and fig. S3H). Whereas ruptured micronuclei were more likely to be near mitochondria, the same was not true for peroxisomes (fig. S4, A and B), another source of cellular ROS (25). Catalase limits ROS leakage outside of peroxisomes (33, 34). Accordingly, inducing peroxisomal ROS through fatty acid addition did not enhance micronuclear rupture in the presence of catalase (35, 36), whereas suppression of peroxisomal ROS production through inhibition of acylCoA oxidase 1 (ACOX1) did not reduce rupture (fig. S4, C to I). Thus, mitochondria-derived ROS were shown to be an important contributor to micronuclear rupture.

Micronuclear rupture through an ESCRT-III-independent function of CHMP7

We then asked if ROS disrupt the function of the ESCRT-III nuclear membrane repair complex, which is known to localize to micronuclei (22) (Fig. 2A). Prior reports have suggested that overzealous function of the ESCRT-III is a potential mechanism for inducing micronuclear rupture (21). We generated HeLa cells stably expressing a doxycycline-inducible Cas9 and single-guide RNA against *CHMP7*, the scaffolding protein of the complex, as well as charged multivesicular protein 2a (*CHMP2A*) and 4b (*CHMP4B*), two essential ESCRT-III subunits (Fig. S5A) (37). Inducible knockout (KO) of *CHMP7* completely abolished ROS-induced micronuclear rupture (Fig. 2B). However, KO of either *CHMP2A* or *CHMP4B* had no impact on this process (Fig. 2B and fig. S5, B to M). Furthermore, in untreated or vehicle-treated conditions, depletion of CHMP7 alone reduced the basal incidence of ruptured micronuclei (fig. S6, A to D). Moreover, treatment of *CHMP7*-KO cells with NAC did not reduce micronuclear rupture further (Fig. 2C and fig. S6, E and F). Constitutive expression of CRISPR-resistant [bearing a nonsense mutation in

the protospacer adjacent motif (PAM) sequence, hereafter PAM*], CHMP7 fully restored ROS-induced micronuclear rupture in *CHMP7*-KO cells, along with the protective effect of NAC treatment on micronuclei (Fig. 2, D and E). Thus, we found that CHMP7 protein mediates ROS-induced micronuclear rupture independently from its canonical ESCRT-III function.

ROS promoted micronuclear CHMP7 accumulation

Using high-resolution imaging of CHMP7-green fluorescent protein (GFP)–expressing HeLa cells, we observed that ROS promote CHMP7 accumulation mostly in lamin B–positive (lamin B^+) (i.e., intact) micronuclei (Fig. 2, F and G). Similar results were obtained by staining for endogenous CHMP7 in thyroid cancer cells (fig. S6, G to J). This observation was corroborated by live-cell imaging, whereby CHMP7 localization to micronuclei preceded the loss of micronuclear compartmentalization (fig. S7). Conversely, treatment with NAC reduced micronuclear CHMP7 accumulation (Fig. 2H). The export of CHMP7 from the nucleus depends on the nuclear export receptor, the exportin XPO1, and the latter's recognition of the nuclear export sequence (NES) on CHMP7 (5). ROS can inhibit nuclear export through O-linked *N*-acetylglucosamine ligation (O-Glc-NACylation) of nucleoporins (Nup), thus increasing their binding to XPO1 and limiting its mobility, which is critical to its export function (38). This led us to ask whether ROS disrupt CHMP7 export from the micronucleus through inhibition of XPO1-dependent export. Indeed, inducing ROS increased O-Glc-NAC signal at the nuclear membranes (fig S8, A to C). We then performed liquid chromatography–mass spectrometry (LC-MS) on micronuclei purified (39, 40) from cells that had been treated with H_2O or H_2O_2 and found a relative enrichment of XPO1 in micronuclei under elevated ROS conditions (fig. S8, D and E, and table S3). Furthermore, in cells transiently expressing XPO1 fused to a yellow fluorescent protein (YFP) under oxidative conditions, we observed an accumulation of XPO1 at the micronuclear envelope before rupture, suggesting increased aberrant binding that interferes with its export function (fig. S8, F to J).

We next treated HeLa and U2OS cells with a pan-nuclear export inhibitor, leptomycin B (LMB), or the XPO1-specific inhibitor selinexor. Treatment with either drug led to a significant increase in micronuclear rupture, abolished the ability of ROS to further increase rupture frequency, and completely prevented NAC-induced stabilization of the micronuclear envelope (Fig. 2 I and fig. S8, K to L). Conditional KO of *CHMP7*—but not *CHMP4B*—abolished the effect of selinexor on micronuclear rupture (Fig. 2J). Next, we expressed PAM* CHMP7 with either a mutated or truncated nuclear export sequence (NES* and ΔNES, respectively) (21) in cells bearing a conditional *CHMP7* KO (Fig. 2K). Expression of either mutant led to constitutive accumulation of CHMP7 in micronuclei and induced a ROS- and ESCRT-III–independent increase in micronuclear rupture, abolishing the membrane stabilizing effect of NAC (Fig. 2, L and M, and fig. S9, A to F). We thus showed that failing to export CHMP7 mediates ROS-dependent increase in micronuclear rupture.

CHMP7 induced rupture through aggregation and binding with LEMD2

Given the dispensability of ESCRT-III function for ROS-induced micronuclear rupture, we sought to understand how CHMP7, a protein without any known membrane remodeling function on its own, collapses micronuclei. Using high-resolution microscopy and three-dimensional (3D) reconstruction, we found that $CHMP7^+$ micronuclei are characterized by an increased nuclear lamina deformation, suggesting binding to lamina components (Fig. 3, A and B). To identify putative ROS-dependent CHMP7 binding partners in micronuclei, we immunoprecipitated CHMP7 from micronuclei purified from cells treated with H_2O_2 or NAC and performed LC-MS on the pulldown (Fig. 3, C and D, and table S4). ROS led to a shift in CHMP7 binding: Under NAC conditions, CHMP7 bound the ESCRT-III repair complex subunits, CHMP2A and CHMP4B, a finding we confirmed by immunoblot on CHMP7 pulled down from whole-cell lysates (Fig. 3D and fig. S10, A and B). Conversely, under elevated ROS conditions, CHMP7 was more likely to bind LEMD2, an inner nuclear membrane structural protein, as confirmed by LEMD2 reciprocal pull down (Fig. 3D and fig. S10, B and C).

We thus hypothesized that ROS-dependent CHMP7-LEMD2 interaction induced micronuclear envelope deformation and collapse (Fig. 3E and fig. S10D). To test this, we generated inducible *LEMD2* KO in HeLa iCas9 cells. LEMD2 depletion led to protection from ROS-induced micronuclear rupture and fully rescued micronuclear integrity to levels seen with NAC treatment (Fig. 3, F to H, and fig. S10, E to G). Moreover, micronuclear deformation was reduced under both *CHMP7* KO and *LEMD2* KO conditions, and we confirmed these findings with atomic force microscopy images of purified micronuclei (fig. S10, H to J). We then rescued inducible *LEMD2* KO with PAM* LEMD2 or with a truncated version of LEMD2 that lacks the CHMP7 binding domain (CBD, referred to as ΔCter LEMD2) (Fig. 3I) (41, 42). Complementation of *LEMD2* KO with ΔCter LEMD2 led to restoration in micronuclear envelope integrity, ROS-insensitivity, and overall reduced CHMP7 retention in micronuclei (Fig. 3, J and K, and fig. S11A). This result suggests that micronuclear retention of CHMP7 is partially dependent on export inhibition as well as on its concentration through binding to LEMD2. Furthermore, micronuclei in ΔCter LEMD2–expressing cells were also resistant to nuclear export inhibition or overexpression of CHMP7 NES*, which accumulated in micronuclei and would normally promote significant micronuclear envelope collapse (Fig. 3, J and K, compared with Fig. 2, K to M, and fig. S11B). Thus, we found that the accumulation of CHMP7 in micronuclei is necessary but not sufficient to induce rupture and that CHMP7-LEMD2 binding is required. Accordingly, complementation of *CHMP7* KOs with LEMD2-binding domain (LBD)–deficient mutants [referred to as ΔCter and ΔNter CHMP7 (41)] abolished ROS-dependent micronuclear rupture and membrane deformation (Fig. 3, L and M, and fig. S11, C and D).

CHMP7-dependent micronuclear rupture was inhibited by cyclin-dependent kinase 1

Our CHMP7-IP analysis revealed that in addition to ESCRT-III components, NAC treatment promotes CHMP7–cyclin dependent kinase 1 (CDK1) interaction (Fig. 3D and table

S4). CDK1-mediated phosphorylation of CHMP7 is known to impact its interaction with LEMD2 (42). Phosphorylation of serine 3 (S3) and serine 441 (S441) on CHMP7 impedes its binding to LEMD2 in the context of its canonical ESCRT-III function (42) (fig. S12A). To test whether ROS affect CHMP7 phosphorylation, we conducted a phosphoproteomic analysis of CHMP7 after immunoprecipitating the protein from cells treated with either H_2O_2 or NAC. Increased ROS levels led to a significant reduction in CHMP7-S3 phosphorylation (fig. S12, B to E). We noted a significantly reduced CDK1 activity in micronuclei compared with primary nuclei as evidenced by reduced phosphorylation of retinoblastoma protein (pRb) staining in the former (fig. S12, F to I). We then used a CDK1-specific inhibitor, Ro3306, at two different concentrations (1 μM and 10 μM) to evaluate the impact of CDK1 activity on micronuclear rupture. Only the high-dose inhibition led to a cell-cycle arrest; however, at 1-μM doses, Ro3306 still led to a significant reduction of pRb in micronuclei (fig. S12, L to O). In line with this finding, pharmacologic inhibition of CDK1 at either concentration led to a significant increase in micronuclear rupture (fig. S13 A and B). The effect of the CDK1 inhibitor was fully rescued upon treatment with NAC and further exacerbated upon nuclear export inhibition with selinexor (fig. S13, C and D), suggesting that preventing CHMP7-S3 and -S441 phosphorylation enhances its binding to LEMD2 rather than its accumulation in micronuclei. As such, treatment with Ro3306 did not promote CHMP7 accumulation in micronuclei (fig. S13, E and F).

To complement our pharmacological findings, we expressed CHMP7 protein containing phosphorylation-resistant mutants in either serine residues (e.g., S3A CHMP7 and S441A CHMP7) or in both residues (P*CHMP7) in otherwise *CHMP7* KO cells (fig. S13G) (in the mutants, we indicated the location of the original amino acid residue and the residue with which we substituted it; for example, S3A indicates that serine at position 3 was replaced with alanine). Expression of any of these mutants led to an increase in micronuclear rupture, which was rescued upon NAC treatment (fig. S13, H and I), mirroring our pharmacological findings. Collectively, these results supported the notion that phosphorylation-mediated disruption of CHMP7-LEMD2 binding is a secondary mechanism through which ROS exacerbate micronuclear rupture and that this mechanism is dependent on the accumulation of CHMP7 in micronuclei. CHMP7 phosphoproteomic analysis revealed additional and reciprocal ROS-dependent phosphorylation sites in CHMP7 (e.g., S410, S417, and S429), some of which were putative targets of kinases in the nuclear factor κB (NF-κB) pathway, invoking a potential regulatory role (fig. S12, C and D) (43).

ROS promoted CHMP7 oligomerization and cysteine oxidation

The physical deformation of $CHMP7^+$ micronuclei was reminiscent of a potential underlying mechanism that involved CHMP7 aggregation (Fig. 3, A and E). H_2O_2 reacts with thiols (−SH) to form disulfides (−S–S) (fig. S14) (30, 44). We hypothesized that mitochondria-derived H_2O_2 reacts with the thiol moieties of one or more of the five cysteinyl residues of CHMP7 to form oligomers that interact with LEMD2, thus deforming micronuclei. To test this, we first asked whether the presence of H_2O_2 could perturb CHMP7 dynamics in micronuclei-localized aggregates. Our analysis of fluorescence recovery after photobleaching in live cells expressing CHMP7-GFP showed that when cells were exposed to H_2O_2, micronuclear CHMP7 aggregates experienced less protein exchange between

diffusible and bound CHMP7, indicating an enhanced binding strength and longevity (fig. S14, A to C).

Next, we analyzed the impact of H_2O_2 treatment on the higher-order structure of purified recombinant CHMP7 by using nonreducing gel electrophoresis. The addition of H_2O_2 to monomeric CHMP7 resulted in two major modifications within 30 s of the reaction: the formation of a slower-migrating form of CHMP7 (CHMP7′) and the formation of CHMP7 tetramers. As the reaction proceeded, CHMP7’ and the CHMP7 tetramers were consumed to form higher oligomers that dominated the reaction by 8 min (Fig. 3, N and O, and fig. S14D). These high–molecular weight isoforms were abolished upon treatment with the reducing agent dithiothreitol (DTT), indicating that the oligomers were stabilized by intermolecular disulfide bonds (Fig. 3N). It is also likely that CHMP7’ contained an intramolecular disulfide bond that facilitated intermolecular thiol-disulfide exchange to form the various oligomers (fig. S14E). These reactions are nonspecific and sequence-independent and can thus happen between CHMP7 and other proteins with cysteinyl residues. Thus, the presence of several cysteinyl residues in LEMD2, together with the absence of such residues in both CHMP2A and CHMP4B, might provide an explanation for the shift in CHMP7 binding partners observed upon ROS increase (Fig. 3D). Our findings do not preclude the possibility of additional ROS-mediated aggregation mechanisms, such as the activation of transglutaminase 3 (TGM3) (45–47); our proteomic analysis of micronuclei identified TGM3 among the CHMP7-binding partners, yet its interaction remained unaltered by ROS.

To test whether CHMP7’s cysteinyl residues participate in ROS-induced micronuclear rupture, we generated a CHMP7 mutant in which all CHMP7 cysteines (C187, C191, C265, C273, and C355) were substituted with serine residues (CHMP7 Cys*) (Fig. 3P). Expression of this mutant in *CHMP7*-KO cells abolished the effect of ROS and NAC on micronuclear rupture (Fig. 3, Q and R). Taken together, these observations supported the hypothesis that cysteinyl residues belonging to CHMP7 react with mitochondrially derived H_2O_2 to form disulfide-bonded oligomers that associate with LEMD2 to further destabilize micronuclear membranes (fig. S14F). This interaction seemed to occur through a distinct mechanism separate from the physiological CHMP7-LEMD2 binding (48), hereafter termed “pathological interaction.”

Defective membrane repair in micronuclei

Another important distinction between micronuclei and primary nuclei is the efficiency by which membranes are repaired upon rupture. Live-cell imaging of micronuclei revealed only a single repair event out of 187 micronuclei that were tracked with five independent markers of micronuclear rupture (fig. S15A). Although ESCRT-III-mediated repair is more effective in primary nuclei (1, 49), recent evidence from Martin *et al.* (50) suggests that selective ROS-mediated recruitment of the autophagy factor and ubiquitin-binding protein p62 (encoded by *SQSTM1*) to micronuclei inhibits normal ESCRT-III function, hampering any chances of repair. In line with this evidence, H_2O_2 reduced the cellular levels of the ESCRT-III proteins, especially of CHMP2A, but this effect was rescued upon p62 depletion (fig. S15, B to D). Similarly, p62 loss increased $CHMP7^+$ micronuclei. However, pathologic ROS-mediated CHMP7 accumulation in micronuclei was independent

of p62 (fig. S15, E to G), suggesting that the impact of p62 on CHMP7 levels is likely through its ESCRT-III–related functions. Thus, micronuclei in cancer cells may suffer from increased rupture through ROS-dependent CHMP7-LEMD2 binding coupled to reduced repair through p62-mediated inhibition of canonical ESCRT-III function, potentially explaining the irreversibility of micronuclear collapse (fig. S15H).

ROS promoted micronuclei-dependent chromosome shattering

A consequence of micronuclear rupture is extensive DNA damage that leads to the shattering of the enclosed chromosomes (14, 51, 52). These chromosomal fragments are subsequently repaired in an error-prone manner leading to complex chromosomal rearrangements, also known as chromothripsis (17, 52–54). To determine whether ROS promotes chromosome shattering as an intermediate step in chromothripsis, we used a doxycycline and auxin (DOX/IAA)–inducible Y chromosome mis-segregation system established in otherwise chromosomally stable DLD-1 colorectal cancer cells to generate chromosome-specific micronuclei (52, 53). As expected, treatment with ROS promoted the rupture of Y chromosome–containing micronuclei, whereas rupture was reduced by exposure to NAC (fig. S16, A and B). Upon DOX/IAA treatment, up to ~20% of mitotic spreads analyzed by DNA fluorescence in situ hybridization contained visibly shattered Y chromosomes (fig. S16, C and D). Chromosome shattering was significantly suppressed by treatment with NAC or small interfering RNA–mediated depletion of CHMP7 (fig. S16D). Thus, suppression of basal ROS or loss of CHMP7 prevented chromosome shattering due to micronuclear rupture.

Hypoxia-derived ROS promoted micronuclear collapse

Tumor hypoxia is a common cause of ROS in cancer. Hypoxia is typically associated with reduced availability of oxygen, which is substituted at its binding sites at the mitochondrial ETC complex IV by nitric oxide, blocking electron transport. The resulting increased leakage of electrons from complexes I and III is responsible for the production of ROS, as previously explained (55). We asked whether hypoxia regulates micronuclear integrity through ROS. Indeed, culture of U2OS and HeLa cells in 1% O_2 led to a significant increase in micronuclear rupture compared with that occurring in cells grown under atmospheric conditions (Fig. 4A and fig. S17A). HeLa cells grown under hypoxic conditions exhibited increased localization of CHMP7-GFP in micronuclei (fig. S17B). Treatment of cells grown under hypoxic conditions in the presence of NAC led to a significant rescue of micronuclear rupture (fig. S17C), supporting the notion that increased micronuclear rupture in response to hypoxia is driven by ROS. To link hypoxia mechanistically to CHMP7-mediated micronuclei disruption, we performed conditional KO of *CHMP7* and *LEMD2* in cells grown in hypoxia and observed a complete restoration of micronuclear integrity under hypoxic conditions to levels that were even lower than those seen in cells grown under normoxic conditions (Fig. 4B). As expected, hypoxia-induced micronuclear rupture was restored upon addition of PAM* CHMP7 and PAM* LEMD2 in otherwise *CHMP7* KO and *LEMD2* KO cells, respectively (Fig. 4B). Expression of CHMP7 NES* in *CHMP7* KO cells led to a significant increase in micronuclear rupture under normoxic conditions

and abolished any additional impact of hypoxia (Fig. 4B). Thus, we showed that hypoxia-induced micronuclear rupture is mediated by CHMP7.

Hypoxia was associated with micronuclear rupture in human cancers

To examine the impact of hypoxia on micronuclear integrity in human tumors, we analyzed two independent cohorts of human high-grade serous ovarian cancer (HGSOC) and human papillomavirus-induced (HPV^+) head and neck squamous cell carcinoma (HNSCC). In the HGSOC cohort (18), we investigated whether the propensity for micronuclear rupture correlated with proximity to the tumor core, given the established relationship between increased hypoxia and distance from the tumor edge (56). Indeed, we observed a distance-dependent increase in micronuclear rupture away from the tumor edge as evidenced by increased cGAS staining in micronuclei (Fig. 4, C and D, and fig. S17, D and E). In the HNSCC tumor cohort, hypoxia was radiographically inferred from ^{18}F-fluoromisonidazole positron emission tomography imaging, and the tumors were stratified as either normoxic or hypoxic (57). Not only did hypoxic tumors display more CHMP7+ micronuclei, but they also exhibited a three- to fourfold increase in micronuclear rupture when compared with their normoxic counterparts (Fig. 4, E and H, and fig. S17F) further supporting the notion that tumor hypoxia is associated with increased micronuclear rupture in human cancers.

Discussion

Our data suggest that the physical proximity of mitochondria to micronuclei exposes the micronuclei to elevated ROS levels. This prevents CHMP7 export from micronuclei while promoting the formation of higher-order CHMP7 structures that associate with LEMD2, disrupting micronuclear envelopes. These ROS-dependent defects in nuclear architecture are likely to be conserved across micronuclei and primary nuclei. Yet, the difference in size and curvature and reduced lamin protein levels (16, 20), as well as defective nuclear pore complexes in micronuclei (15), might predispose the latter to rupture at lower ROS thresholds compared with primary nuclei.

We thus show that mitochondrial ROS disrupt micronuclear integrity through multiple concerted means. These include (i) inducing aberrant CHMP7 localization in micronuclei; (ii) promoting the pathological interaction of CHMP7 and LEMD2; (iii) promoting physiological CHMP7-LEMD2 binding through reduction in CDK1-mediated CHMP7 phosphorylation; (iv) inducing higher order structures of CHMP7 through, among other possible mechanisms, cysteine oxidation; and (v) reducing micronuclear membrane repair through recruitment of p62 and subsequent degradation of ESCRT-III. As shown by Martin *et al.* (50), ROS promote p62 activity through cysteine oxidation and polymerization, a mechanism analogous to what we demonstrated for CHMP7.

Lastly, our data provide an important mechanistic link between tumor hypoxia and key processes that drive cancer progression, such as pro-tumor inflammation, chromosomal abnormalities, and epigenetic alterations (17, 18, 58, 59). How hypoxia leads to these abnormalities had been poorly understood. Given the well-established role of micronuclear rupture in all of these processes (14, 18, 19, 59), our work suggests that micronuclear

rupture induced by hypoxia might be a key mechanism by which hypoxia can drive tumor progression (25). Perhaps targeting pathologic processes spurred by ruptured micronuclei might represent a therapeutic goal in tumors characterized by extensive hypoxia.

Methods summary

The experiments were performed with publicly available cell lines. The inducible KOs were generated with CRISPR-Cas9 technology: HeLa cells expressing inducible Cas9, selected guide RNAs, and Cas9-resistant mutants were generated with lentiviral transduction and antibiotic selection. HeLa cells expressing NLS-RFP, CHMP7-GFP, cGAS-GFP, LEMD2-mCherry, and H2B-iRFP were generated with lentiviral transduction followed by antibiotic selection and fluorescence activated cell sorting. Micronuclei were purified from CHMP7-GFP–expressing HeLa cells as previously described (39) and further processed for CHMP7 immunoprecipitation by using anti-GFP antibody bound to magnetic G–protein coupled beads (for identification of CHMP7-binding partners through proteomics), or for total proteomics. Whole-cell lysates of HeLa cells expressing CHMP7-GFP were processed for CHMP7 immunoprecipitation by using GFP-trap agarose beads for CHMP7 phosphoproteomics and for immunoblot analysis of CHMP7-binding partners. Cell-cycle analysis was performed through flow cytometry by using 4′,6-diamidino-2-phenylindole (DAPI) content to discriminate between the cell-cycle phases, and in vitro polymerization experiments were performed by using commercially available recombinant CHMP7. Imaging was performed with commercially available microscopes, antibodies, and dyes; all drugs and pharmacological treatments are also commercially available. Plasmids and DNA sequences, when not commercially available, are provided in the supplementary materials. Image analysis was performed on ImageJ or on Imaris, and statistical analysis was carried out in GraphPad Prism. Sketches were generated with Biorender. com. For more a detailed explanation of experimental procedures, analysis, and custom macros, see the supplementary materials.

Supplementary Material

Refer to Web version on PubMed Central for supplementary material.

ACKNOWLEDGMENTS

We thank members of the Bakhoum Lab and especially D. Al-Rawi and lab alumnus N. Vashi for useful discussions and feedback. We also thank P. Guasp Baratech at Memorial Sloan Kettering Cancer Center (MSKCC) for discussion and technical help. We wish to thank P. Van Loo and A. R. Lynch for useful discussions and exchange of ideas. We are grateful to the Cheeseman, Fearon, and Chan Labs for sharing cell lines and to the Abdel-Wahab lab for sharing their XPO-YFP plasmid. We thank staff at the MSKCC integrated genomics, bioinformatic, flow cytometry, and molecular cytology core facilities. Lastly, we are grateful to H. Lacks (now deceased) and to her surviving family members for their contributions to this research.

Funding:

M.D.B. is supported by an American-Italian Cancer Foundation Post-Doctoral Research Fellowship. S.F.B. is supported by NIH DP5OD026395, NCI P50CA247749, R01CA256188-01, the Congressionally Directed Medical Research Program, the Burroughs Wellcome Fund, the Josie Robertson Foundation, and the Mark Foundation for Cancer Research. Y.C. is supported by the Center for Experimental Immuno-Oncology (EIO) Scholars Program from at MSKCC. A.S.A. is supported by the PhRMA Foundation, and C.H. is supported by the Radenac Nicola Foundation. Work in the Santaguida lab is supported by grants from the Italian Association for Cancer Research

(AIRC-MFAG 2018 – ID. 21665 project and AIRC Bridge Grant 2023 – ID. 29228 project), Ricerca Finalizzata (GR-2018-12367077), Fondazione Cariplo, the Rita-Levi Montalcini program from MIUR, and the Italian Ministry of Health with Ricerca Corrente 5 × 1000 funds.

Data and materials availability:

All data are available in the main text, the supplementary materials, or on Dryad (60), following MIBBI (Minimum Information for Biological and Biomedical Investigations) guidelines.

REFERENCES AND NOTES

1. Denais CM et al. Nuclear envelope rupture and repair during cancer cell migration. Science 352, 353–358 (2016). doi: 10.1126/science.aad7297; [PubMed: 27013428]
2. Halfmann CT, Roux KJ, Barrier-to-autointegration factor: A first responder for repair of nuclear ruptures. Cell Cycle 20, 647–660 (2021). doi: 10.1080/15384101.2021.1892320; [PubMed: 33678126]
3. Raab M et al. ESCRT III repairs nuclear envelope ruptures during cell migration to limit DNA damage and cell death. Science 352, 359–362 (2016). doi: 10.1126/science.aad7611; [PubMed: 27013426]
4. Maciejowski J, Hatch EM, Nuclear Membrane Rupture and Its Consequences. Annu. Rev. Cell Dev. Biol 36, 85–114 (2020). doi: 10.1146/annurev-cellbio-020520-120627; [PubMed: 32692592]
5. Thaller DJ et al. An ESCRT-LEM protein surveillance system is poised to directly monitor the nuclear envelope and nuclear transport system. eLife 8, e45284 (2019). doi: 10.7554/eLife.45284; [PubMed: 30942170]
6. Gu M et al. LEM2 recruits CHMP7 for ESCRT-mediated nuclear envelope closure in fission yeast and human cells. Proc. Natl. Acad. Sci. U.S.A 114, E2166–E2175 (2017). doi: 10.1073/pnas.1613916114; [PubMed: 28242692]
7. Hanahan D, Weinberg RA, Hallmarks of cancer: The next generation. Cell 144, 646–674 (2011). doi: 10.1016/j.cell.2011.02.013; [PubMed: 21376230]
8. Lukow DA et al. Chromosomal instability accelerates the evolution of resistance to anti-cancer therapies. Dev. Cell 56, 2427–2439.e4 (2021). doi: 10.1016/j.devcel.2021.07.009; [PubMed: 34352222]
9. Bakhoum SF, Cantley LC, The Multifaceted Role of Chromosomal Instability in Cancer and Its Microenvironment. Cell 174, 1347–1360 (2018). doi: 10.1016/j.cell.2018.08.027; [PubMed: 30193109]
10. Bakhoum SF, Landau DA, Chromosomal Instability as a Driver of Tumor Heterogeneity and Evolution. Cold Spring Harb. Perspect. Med 7, a029611 (2017). doi: 10.1101/cshperspect.a029611; [PubMed: 28213433]
11. Ippolito MR et al. Gene copy-number changes and chromosomal instability induced by aneuploidy confer resistance to chemotherapy. Dev. Cell 56, 2440–2454.e6 (2021). doi: 10.1016/j.devcel.2021.07.006; [PubMed: 34352223]
12. Di Bona M, Bakhoum SF, Micronuclei and Cancer. Cancer Discov. 14, 214–226 (2024). doi: 10.1158/2159-8290.CD-23-1073; [PubMed: 38197599]
13. Ganem NJ, Godinho SA, Pellman D, A mechanism linking extra centrosomes to chromosomal instability. Nature 460, 278–282 (2009). doi: 10.1038/nature08136; [PubMed: 19506557]
14. Crasta K et al. DNA breaks and chromosome pulverization from errors in mitosis. Nature 482, 53–58 (2012). doi: 10.1038/nature10802; [PubMed: 22258507]
15. Liu S et al. Nuclear envelope assembly defects link mitotic errors to chromothripsis. Nature 561, 551–555 (2018). doi: 10.1038/s41586-018-0534-z; [PubMed: 30232450]
16. Hatch EM, Fischer AH, Deerinck TJ, Hetzer MW, Catastrophic nuclear envelope collapse in cancer cell micronuclei. Cell 154, 47–60 (2013). doi: 10.1016/j.cell.2013.06.007; [PubMed: 23827674]

17. Zhang CZ et al. Chromothripsis from DNA damage in micronuclei. Nature 522, 179–184 (2015). doi: 10.1038/nature14493; [PubMed: 26017310]
18. Agustinus AS et al. Epigenetic dysregulation from chromosomal transit in micronuclei. Nature 619, 176–183 (2023). doi: 10.1038/s41586-023-06084-7; [PubMed: 37286593]
19. Papathanasiou S et al. Heritable transcriptional defects from aberrations of nuclear architecture. Nature 619, 184–192 (2023). doi: 10.1038/s41586-023-06157-7; [PubMed: 37286600]
20. Joo YK et al. ATR promotes clearance of damaged DNA and damaged cells by rupturing micronuclei. Mol. Cell 83, 3642–3658.e4 (2023). doi: 10.1016/j.molcel.2023.09.003; [PubMed: 37788673]
21. Vietri M et al. Unrestrained ESCRT-III drives micronuclear catastrophe and chromosome fragmentation. Nat. Cell Biol 22, 856–867 (2020). doi: 10.1038/s41556-020-0537-5; [PubMed: 32601372]
22. Willan J et al. ESCRT-III is necessary for the integrity of the nuclear envelope in micronuclei but is aberrant at ruptured micronuclear envelopes generating damage. Oncogenesis 8, 29 (2019). doi: 10.1038/s41389-019-0136-0; [PubMed: 30988276]
23. Mammel AE, Huang HZ, Gunn AL, Choo E, Hatch EM, Chromosome length and gene density contribute to micronuclear membrane stability. Life Sci. Alliance 5, e202101210 (2021). doi: 10.26508/lsa.202101210; [PubMed: 34789512]
24. Chen Q, Vazquez EJ, Moghaddas S, Hoppel CL, Lesnefsky EJ, Production of reactive oxygen species by mitochondria: Central role of complex III. J. Biol. Chem 278, 36027–36031 (2003). doi: 10.1074/jbc.M304854200; [PubMed: 12840017]
25. Wu K, El Zowalaty AE, Sayin VI, Papagiannakopoulos T, The pleiotropic functions of reactive oxygen species in cancer. Nat. Cancer 5, 384–399 (2024). doi: 10.1038/s43018-024-00738-9; [PubMed: 38531982]
26. Zhang X et al. Induction of mitochondrial dysfunction as a strategy for targeting tumour cells in metabolically compromised microenvironments. Nat. Commun 5, 3295 (2014). doi: 10.1038/ncomms4295; [PubMed: 24548894]
27. To TL et al. A Compendium of Genetic Modifiers of Mitochondrial Dysfunction Reveals Intra-organelle Buffering. Cell 179, 1222–1238.e17 (2019). doi: 10.1016/j.cell.2019.10.032; [PubMed: 31730859]
28. Mackenzie KJ et al. cGAS surveillance of micronuclei links genome instability to innate immunity. Nature 548, 461–465 (2017). doi: 10.1038/nature23449; [PubMed: 28738408]
29. Issels RD, Nagele A, Eckert KG, Wilmanns W, Promotion of cystine uptake and its utilization for glutathione biosynthesis induced by cysteamine and N-acetylcysteine. Biochem. Pharmacol 37, 881–888 (1988). doi: 10.1016/0006-2952(88)90176-1; [PubMed: 3345201]
30. Winterbourn CC, Biological Production, Detection, and Fate of Hydrogen Peroxide. Antioxid. Redox Signal 29, 541–551 (2018). doi: 10.1089/ars.2017.7425; [PubMed: 29113458]
31. Kelso GF et al. Selective targeting of a redox-active ubiquinone to mitochondria within cells: Antioxidant and antiapoptotic properties. J. Biol. Chem 276, 4588–4596 (2001). doi: 10.1074/jbc.M009093200; [PubMed: 11092892]
32. Vidossich P, Alfonso-Prieto M, Rovira C, Catalases versus peroxidases: DFT investigation of H_2O_2 oxidation in models systems and implications for heme protein engineering. J. Inorg. Biochem 117, 292–297 (2012). doi: 10.1016/j.jinorgbio.2012.07.002; [PubMed: 22883961]
33. Lismont C, Nordgren M, Van Veldhoven PP, Fransen M, Redox interplay between mitochondria and peroxisomes. Front. Cell Dev. Biol 3, 35 (2015). doi: 10.3389/fcell.2015.00035; [PubMed: 26075204]
34. Grodzinski B, Butt VS, Hydrogen peroxide production and the release of carbon dioxide during glycollate oxidation in leaf peroxisomes. Planta 128, 225–231 (1976). doi: 10.1007/BF00393233; [PubMed: 24430751]
35. Alsabeeh N, Chausse B, Kakimoto PA, Kowaltowski AJ, Shirihai O, Cell culture models of fatty acid overload: Problems and solutions. Biochim. Biophys. Acta Mol. Cell Biol. Lipids 1863, 143–151 (2018). doi: 10.1016/j.bbalip.2017.11.006; [PubMed: 29155055]

36. Sun S, Cao X, Gao J, C24:0 avoids cold exposure-induced oxidative stress and fatty acid β-oxidation damage. iScience 24, 103409 (2021). doi: 10.1016/j.isci.2021.103409; [PubMed: 34849471]
37. McCullough J, Frost A, Sundquist WI, Structures, Functions, and Dynamics of ESCRT-III/Vps4 Membrane Remodeling and Fission Complexes. Annu. Rev. Cell Dev. Biol 34, 85–109 (2018). doi: 10.1146/annurev-cellbio-100616-060600; [PubMed: 30095293]
38. Crampton N, Kodiha M, Shrivastava S, Umar R, Stochaj U, Oxidative stress inhibits nuclear protein export by multiple mechanisms that target FG nucleoporins and Crm1. Mol. Biol. Cell 20, 5106–5116 (2009). doi: 10.1091/mbc.e09-05-0397; [PubMed: 19828735]
39. Toufektchan E, Maciejowski J, Purification of micronuclei from cultured cells by flow cytometry. STAR Protoc. 2, 100378 (2021). doi: 10.1016/j.xpro.2021.100378; [PubMed: 33778777]
40. Mohr L et al. ER-directed TREX1 limits cGAS activation at micronuclei. Mol. Cell 81, 724–738.e9 (2021). doi: 10.1016/j.molcel.2020.12.037; [PubMed: 33476576]
41. Olmos Y, Perdrix-Rosell A, Carlton JG, Membrane Binding by CHMP7 Coordinates ESCRT-III-Dependent Nuclear Envelope Reformation. Curr. Biol 26, 2635–2641 (2016). doi: 10.1016/j.cub.2016.07.039; [PubMed: 27618263]
42. Gatta AT et al. CDK1 controls CHMP7-dependent nuclear envelope reformation. eLife 10, e59999 (2021). doi: 10.7554/eLife.59999; [PubMed: 34286694]
43. Johnson JL et al. An atlas of substrate specificities for the human serine/threonine kinome. Nature 613, 759–766 (2023). doi: 10.1038/s41586-022-05575-3; [PubMed: 36631611]
44. Miki H, Funato Y, Regulation of intracellular signalling through cysteine oxidation by reactive oxygen species. J. Biochem 151, 255–261 (2012). doi: 10.1093/jb/mvs006; [PubMed: 22287686]
45. Junkunlo K, Söderháll K, Söderháll I, Noonin C, Reactive Oxygen Species Affect Transglutaminase Activity and Regulate Hematopoiesis in a Crustacean. J. Biol. Chem 291, 17593–17601 (2016). doi: 10.1074/jbc.M116.741348; [PubMed: 27339892]
46. Ahvazi B, Steinert PM, A model for the reaction mechanism of the transglutaminase 3 enzyme. Exp. Mol. Med 35, 228–242 (2003). doi: 10.1038/emm.2003.31; [PubMed: 14508061]
47. Lee Z-W et al. Activation of in situ tissue transglutaminase by intracellular reactive oxygen species. Biochem. Biophys. Res. Commun 305, 633–640 (2003). doi: 10.1016/S0006-291X(03)00835-0; [PubMed: 12763041]
48. von Appen A et al. LEM2 phase separation promotes ESCRT-mediated nuclear envelope reformation. Nature 582, 115–118 (2020). doi: 10.1038/s41586-020-2232-x; [PubMed: 32494070]
49. Hatch EM, Hetzer MW, Nuclear envelope rupture is induced by actin-based nucleus confinement. J. Cell Biol 215, 27–36 (2016). doi: 10.1083/jcb.201603053; [PubMed: 27697922]
50. Martin S et al. A p62-dependent rheostat dictates micronuclei catastrophe and chromosome rearrangements. Science 385, eadj7446 (2024). [PubMed: 39208097]
51. Tang S, Stokasimov E, Cui Y, Pellman D, Breakage of cytoplasmic chromosomes by pathological DNA base excision repair. Nature 606, 930–936 (2022). doi: 10.1038/s41586-022-04767-1; [PubMed: 35477155]
52. Ly P et al. Selective Y centromere inactivation triggers chromosome shattering in micronuclei and repair by non-homologous end joining. Nat. Cell Biol 19, 68–75 (2017). doi: 10.1038/ncb3450; [PubMed: 27918550]
53. Ly P et al. Chromosome segregation errors generate a diverse spectrum of simple and complex genomic rearrangements. Nat. Genet 51, 705–715 (2019). doi: 10.1038/s41588-019-0360-8; [PubMed: 30833795]
54. Meyerson M, Pellman D, Cancer genomes evolve by pulverizing single chromosomes. Cell 144, 9–10 (2011). doi: 10.1016/j.cell.2010.12.025; [PubMed: 21215363]
55. Chandel NS et al. Reactive oxygen species generated at mitochondrial complex III stabilize hypoxia-inducible factor-1alpha during hypoxia: A mechanism of O2 sensing. J. Biol. Chem 275, 25130–25138 (2000). doi: 10.1074/jbc.M001914200; [PubMed: 10833514]
56. Vaupel P, Kallinowski F, Okunieff P, Blood flow, oxygen and nutrient supply, and metabolic microenvironment of human tumors: A review. Cancer Res. 49, 6449–6465 (1989). [PubMed: 2684393]

57. Riaz N et al. Precision Radiotherapy: Reduction in Radiation for Oropharyngeal Cancer in the 30 ROC Trial. J. Natl. Cancer Inst 113, 742–751 (2021). doi: 10.1093/jnci/djaa184; [PubMed: 33429428]

58. Li J et al. Non-cell-autonomous cancer progression from chromosomal instability. Nature 620, 1080–1088 (2023). doi: 10.1038/s41586-023-06464-z; [PubMed: 37612508]

59. Bakhoum SF et al. Chromosomal instability drives metastasis through a cytosolic DNA response. Nature 553, 467–472 (2018). doi: 10.1038/nature25432; [PubMed: 29342134]

60. Di Bona M et al. Data from: Micronuclear collapse from oxidative damage, Dryad (2024); 10.5061/dryad.ngf1vhj39.

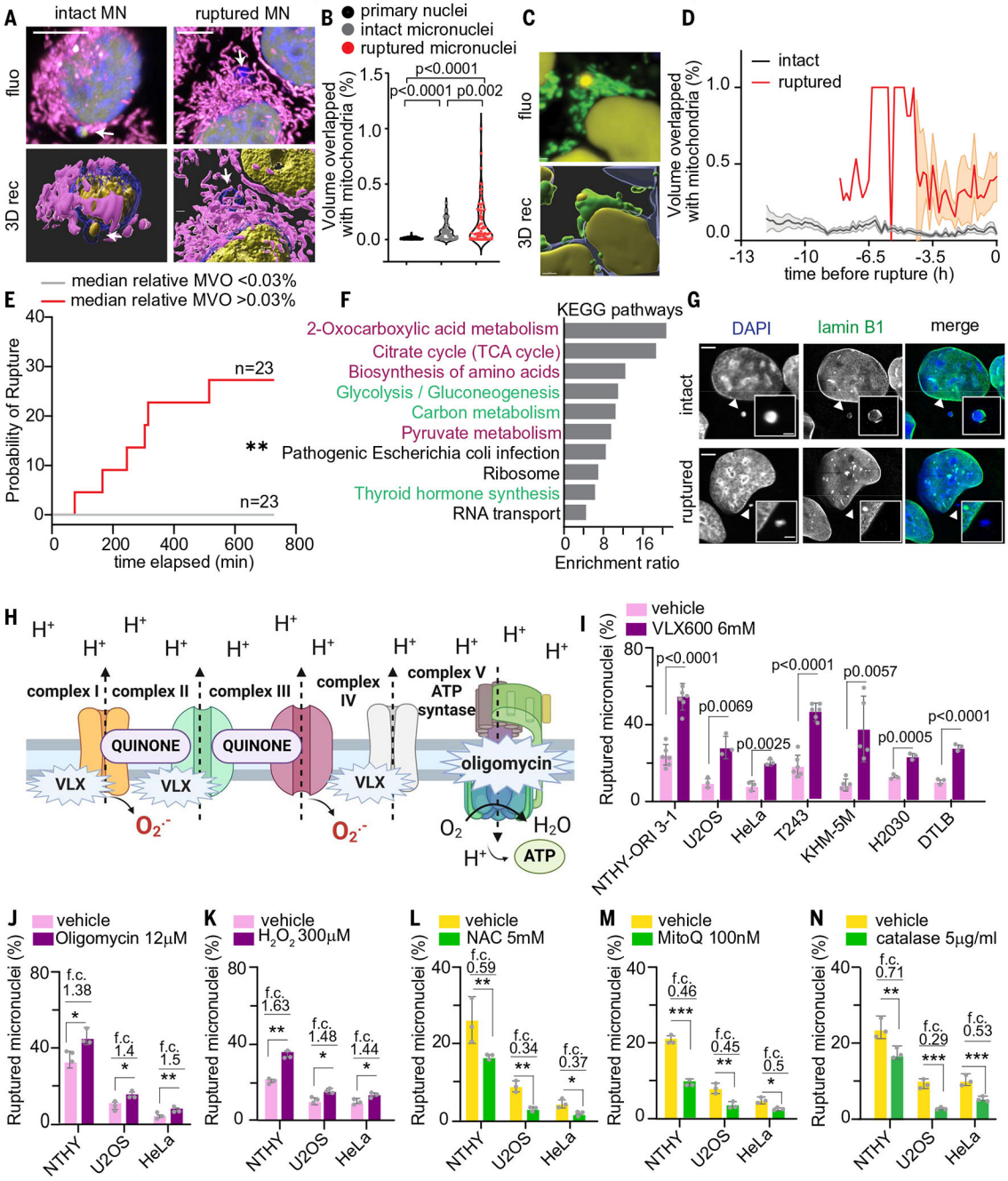

Fig. 1. Mitochondrial ROS are the cause of micronuclear rupture.

(**A**) Representative fluorescence ("fluo," top) and reconstructed 3D ("rec," bottom) images of HeLa cells; yellow indicates nuclear integrity marker (NLS-RFP), magenta indicates mitochondria, and blue indicates DNA (Hoechst 33342). Scale bars, 6 μm. MN, micronucleus. (**B**) Sixty images (A) from three biological replicates analyzed with Imaris. Mitochondria and intact (NLS-RFP+) and ruptured (NLS-RFP−) micronuclei (MNi) and primary nuclei (PN) relative volume overlap. Unpaired Student's *t* test, Welch's correction. (**C**) Representative images of HeLa cells; yellow indicates NLS-RFP, blue indicates H2B-

iRFP, and green indicates mitochondria. Scale bar, 3 μm. (**D**) Thirty total time lapses (C) from three biological replicates analyzed as in (B). Intact (gray) and ruptured (red) MNi-mitochondria relative volume overlap over time (MVO%, percentage of maximum volume overlap). For intact MNi, time 0 indicates imaging end. Mean ± SEM. (**E**) MNi in (D) divided in two populations by the median of MVO%. Log-rank (Mantel-Cox) test (P = 0.0093) and Gehan-Breslow-Wilcoxon test (P = 0.0095). (**F**) Proteins from MNi enriched for rupture (cGAS-GFP+) versus proteins from PN of MDA-MB-231 cells (see materials and methods and table S1). KEGG (Kyoto Encyclopedia of Genes and Genomes) pathway analysis of MNi-enriched proteins (magenta indicates mitochondria-specific processes; green indicates nonexclusive mitochondria-involving processes). (**G**) Intact (top, lamin B+) and ruptured (bottom, lamin B−) MNi in NTHY cells. Scale bar, 3 μm; inset, 1 μm. (**H**) VLX600 and oligomycin targets. (**I** to **N**) Quantification of ruptured MNi (G) after ROS modulation. Minimum of three biological replicates, mean ± SD, unpaired Student's t test. f.c. indicates averages of fold change. (I) Ruptured MNi after 24-hour VLX600 treatment; n = 300 MNi. (J) Ruptured MNi after 4-hour oligomycin treatment; n = 300 MNi. P values: NTHY, 0.0271; U2OS, 0.0388; HeLa, 0.0047. (K) Ruptured MNi after 4-hour H_2O_2 treatment; n = 100 MNi. P values: NTHY, 0.0002; U2OS, 0.0229; HeLa, 0.0124. (L) Ruptured MNi after 24-hour NAC treatment; n = 100 MNi. P values: NTHY, 0.0490; U2OS, 0.0029; HeLa, 0.0104. (M) Ruptured MNi after 24-hour MitoQ (mitoquinone mesylate) treatment; n = 100 MNi. P values: NTHY, 0.0002; U2OS, 0.0094; HeLa, 0.0152. (N) Ruptured MNi after 4-hour catalase treatment; n = 100 MNi. P values: NTHY, 0.0036; U2OS, 0.0006; HeLa, 0.0009.

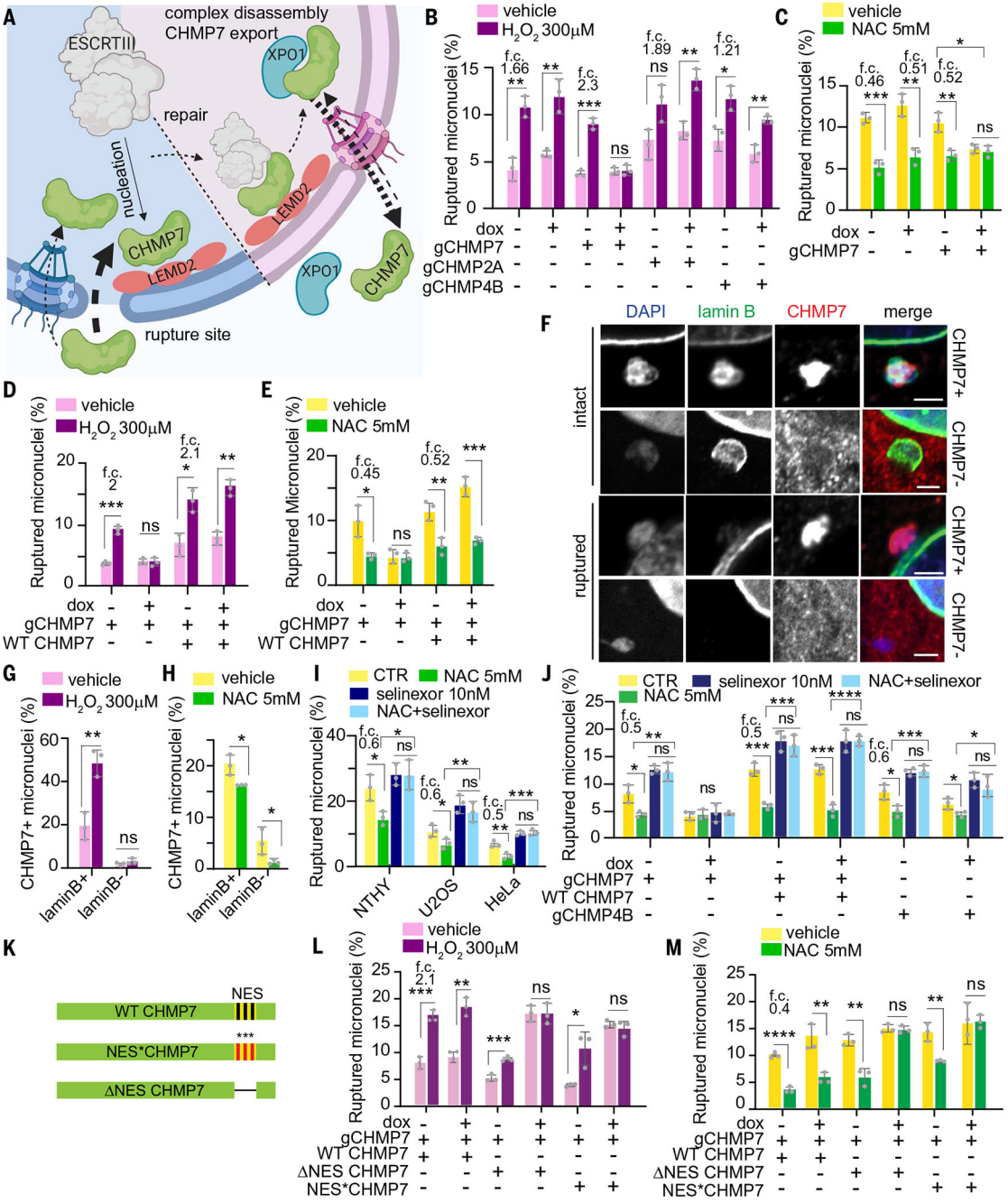

Fig. 2. ROS cause rupture through an ESCRT-III–independent CHMP7 role.

(**A**) CHMP7 moieties diffusing in the nucleus are exported by XPO1. Upon PN rupture (left), CHMP7 saturates XPO1 and binds its partner LEMD2. This nucleates the ESCRT-III complex, which repairs the hole (right), then XPO1 exports all the moieties. (**B** to **E**) Ruptured MNi in HeLa expressing doxycycline (dox, 1 μg/ml, treated for 72 hours)–inducible Cas9 (iCas9) and indicated guide RNAs (gRNAs) with or without PAM* CHMP7 wild type (WT), treated with H_2O_2 or NAC. (B) *P* values for H_2O versus H_2O_2: WTdox−, 0.0024; WTdox, 0.005; gCHMP7dox−, 0.001; gCHMP2Adox, 0.0036;

gCHMP4Bdox−, 0.0122; gCHMP4Bdox, 0.0034. (C) *P* values for H_2O versus NAC: WTdox−, 0.0006;WTdox, 0.0031; gCHMP7dox−, 0.0066; gCHMP7H_2O dox− versus dox, 0.0133. (D) P values for H_2O versus H_2O_2: gCHMP7dox−, 0.0026; CHMP7 WTdox−, 0.0109; CHMP7 WTdox, 0.0011. (E) *P* values for H_2O versus NAC: gCHMP7dox−, 0.0188; CHMP7 WTdox−, 0.0086; CHMP7 WTdox, 0.0009. (**F**) CHMP7+ and CHMP7− intact and ruptured MNi in HeLa. Scale bar, 2 μm. (**G** and **H**) CHMP7+MNi in (F) treated with H_2O_2 or NAC. (G) $P = 0.0053$. (H) *P* values: lamin B+, 0.0463; lamin B−, 0.0442. (**I**) Ruptured MNi treated for 24 hours with selinexor, NAC, or both. *P* values for NTHY: control (CTR) versus NAC, 0.0232; NAC versus both, 0.0101. *P* values for U2OS: CTR versus NAC, 0.0359; NAC versus both, 0.0074. *P* values for HeLa: CTR versus NAC, 0.0021; NAC versus both, 0.0002. (**J**) Ruptured MNi in HeLa as in (B) to (E) treated as in (I). *P* values: gCHMP7dox− CTR versus NAC, 0.0172; gCHMP7dox− NAC versus both, 0.0014; CHMP7 WTdox− CTR versus NAC, 0.0008; CHMP7 WTdox− NAC versus both, 0.0007; CHMP7 WTdox CTR versus NAC, 0.0006; CHMP7 WTdox NAC versus both, <0.0001; gCHMP4Bdox− CTR versus NAC, 0.0226; gCHMP4Bdox− NAC versus both, 0.001; gCHMP4Bdox CTR versus NAC, 0.0279; gCHMP4Bdox NAC versus both, 0.0172. (**K**) Export-deficient CHMP7 mutants. (**L** and **M**) Ruptured MNi in HeLa CHMP7 KO with (K) treated with H_2O_2 or NAC. (L) *P* values for H_2O versus H_2O_2: WTdox−, 0.0004; WTdox, 0.0013; ΔNESdox−, 0.0008; NES*dox−, 0.0193 (M) *P* values for H_2O versus NAC: WTdox−, 0.0019; WTdox, 0.0005; ΔNESdox−, 0.0039; NES*dox−, 0.0049. For (B) to (M), $n = 100$ MNi, three biological replicates, mean ± SD, unpaired Student's *t* test.

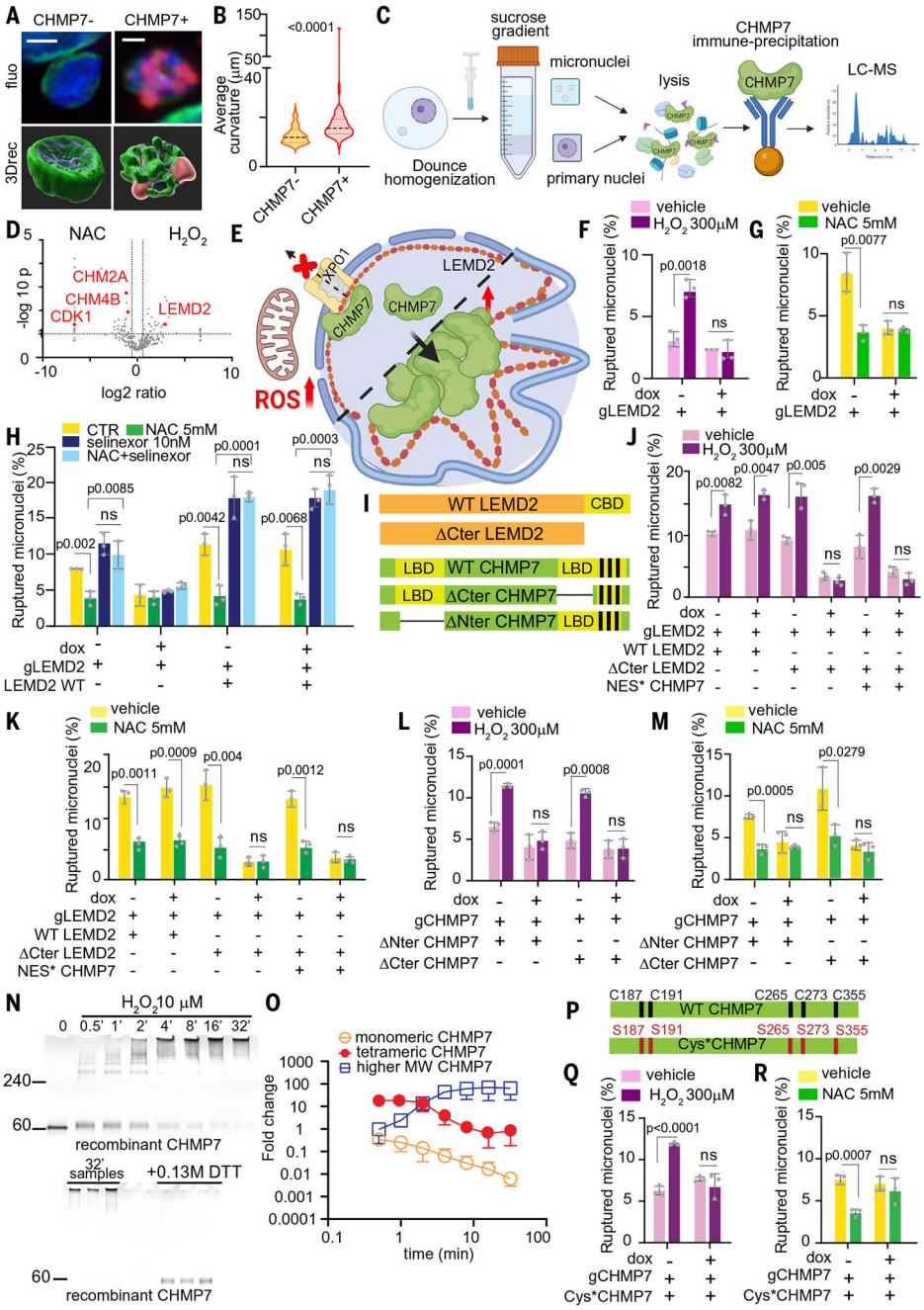

Fig. 3. CHMP7 induces rupture through its binding with LEMD2 and aggregation.

(**A**) Representative CHMP7 (red) + and − MNi. Blue, DAPI; green, lamin B1. Scale bar, 0.5 µm. (**B**) Analysis of (A) with Imaris (see materials and methods) for the average of vertexes mean curvature distribution. $n = 15$ MNi, three biological replicates, Mann-Whitney test. (**C**) Experimental flow of CHMP7 binding partners detection through LC-MS on CHMP7 immunoprecipitated from extracted MNi (39). (**D**) Results of (C), three biological replicates. (**E**) Mitochondrial ROS inhibit XPO1-mediated export of CHMP7, which accumulates in the MNi, oligomerizes and binds LEMD2, pulling it and the lamina until rupture. (**F** and

G) Ruptured MNi in HeLa expressing iCas9 and a guide for LEMD2 treated with H_2O_2 or NAC. (**H**) Ruptured MNi in HeLa LEMD2 KO with or without PAM* LEMD2 WT treated with selinexor, NAC, or both. (**I**) CHMP7- and LEMD2-binding–deficient mutants. (**J** and **K**) Ruptured MNi in HeLa as shown in (F) and (G) expressing the mutants shown in (I) or with ΔCter LEMD2 together with over-expression of CHMP7 NES*, treated with H_2O_2 or NAC. (**L** and **M**) Ruptured MNi in HeLa iCas9 gCHMP7 expressing the mutants shown in (I) treated with H_2O_2 or NAC. (**N**) (Top) Gel electrophoresis of recombinant CHMP7 reacting with 10 μM H_2O_2 for the indicated times. (Bottom) Image shows 32-min reactions as in (top) mixed with 0.13 M DTT to reduce disulfide bonds, showing monomeric CHMP7. (**O**) Quantification of CHMP7 monomers, tetramers, and high–molecular weight oligomers from three biological replicates of experiments conducted as in (N). (**P**) Cysteine-deficient CHMP7 mutant. (**Q** and **R**) Ruptured MNi in HeLa iCas9 gCHMP7 expressing the mutant shown in (P) and treated with H_2O_2 or NAC. For (F) to (R), $n = 100$ MNi, three biological replicates. Mean ± SD, unpaired Student's *t* test.

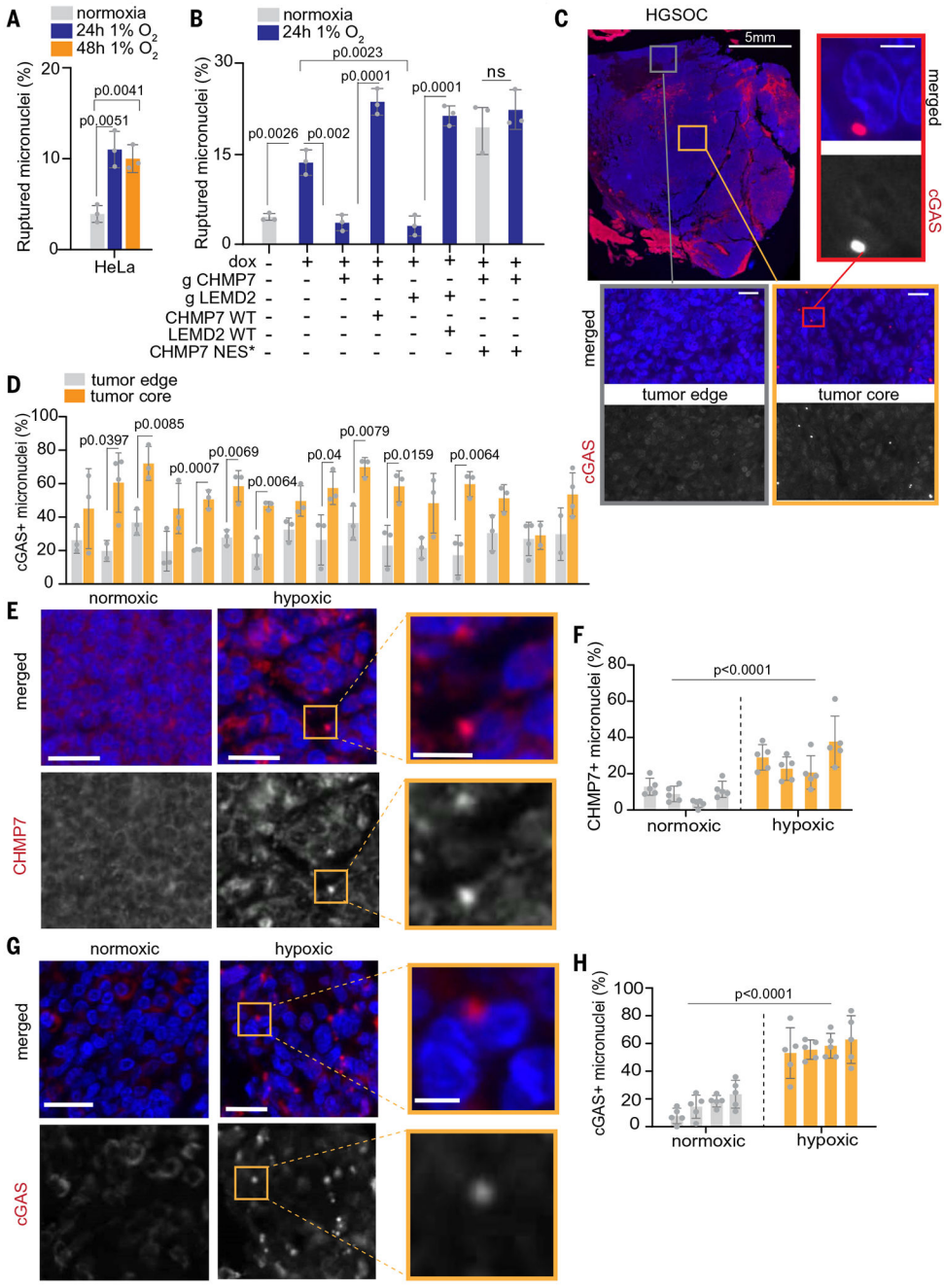

Fig. 4. Hypoxia-derived ROS induce micronuclear collapse.

(**A**) Ruptured MNi in HeLa under hypoxia for the designated times. (**B**) Ruptured MNi in HeLa iCas9 and depleted and/or complemented with the indicated proteins while cultured in atmospheric or 1% O_2 for 24 hours. For (A) and (B), n = 100 MNi, three biological replicates, mean ±SD, unpaired Student's t test. (**C**) Representative images of a high-grade serous ovarian cancer (HGSOC) stained for DAPI (blue) and cGAS (red). Scale bar, 5 mm. (Left) Zoomed sections of the tumor edge and of the tumor core, presumably more hypoxic. Scale bar, 20 μm. (Right) Zoomed images of single micronucleated cells from the tumor

core. Scale bar, 5 μm. (**D**) cGAS+ MNi in six regions of interest (ROI) from 16 different tumors as shown in (E), divided in function of the average ROI distance from the tumor edge. ROI >0.6 mm from the tumor edge are labeled as “tumor core,” and ROI <0.6 mm are labeled “tumor edge.” Unpaired Student’s *t* test, mean ± SD. (**E**) Images of HPV+ head and neck normoxic or hypoxic cancers stained for CHMP7 (red). Scale bar, 20 μm. (Inset) Single micronucleated cell from a hypoxic tumor. Scale bar, 7 μm. (**F**) CHMP7+ MNi in five ROI from each tumor as shown in (E). Significance was calculated by pulling the data together and comparing normoxic versus hypoxic tumors with unpaired Student’s *t* test. The same result is confirmed by one-way analysis of variance (ANOVA) followed by Tukey’s multiple comparisons test. Mean ± SD. (**G**) Images of HPV+ head and neck cancers stained for cGAS (red). Scale bar, 20 μm. (Inset) Single micronucleated cell from a hypoxic tumor. Scale bar, 7 μm. (**H**) cGAS+ MNi in five ROI from each tumor as shown in (G). Significance was calculated by pulling the data together and comparing normoxic versus hypoxic tumors with unpaired Student’s *t* test. The same statistical result is obtained by one-way ANOVA followed by Tukey’s multiple comparisons test. Mean ± SD.